Resonant Platform Response and Vertical Velocity Biases in ADCP Measurements from Quasi-Lagrangian Platforms

Andrey Y. Shcherbina,[a] Eric A. D'Asaro[a]

[a] *Applied Physics Laboratory, University of Washington*

Submitted to the Journal of Atmospheric and Oceanic Technology 13 February 2026

Corresponding author: Andrey Shcherbina, shcher@uw.edu

ABSTRACT: Autonomous surface and subsurface platforms equipped with acoustic Doppler current profilers (ADCPs) are increasingly used to observe ocean velocities, but in the presence of surface waves these measurements can be biased by orbital motion and wave-induced platform tilting. Previous work quantified such biases for idealized platform responses that were in phase with the wave forcing. Here we extend this framework to the general case of a partially resonant platform response, in which the tilt amplitude is enhanced and phase-lagged relative to the waves, as expected for real-world platforms. We derive analytical expressions for wave-induced ADCP biases under arbitrary linear tilt response and show that phase-lagged platform motion generates biases in vertical velocity in addition to previously reported horizontal biases. These vertical biases scale with the imaginary part of the platform tilt transfer function and depend on wave properties, platform depth, and measurement distance. Biases also depend on ADCP beam geometry, alignment with wave propagation, and instrument orientation (upward or downward). Under certain conditions, a five-beam vertical velocity reconstruction can be formed that is unbiased on average and generally outperforms standard four-beam and vertical-beam estimates. The theory is applied to a Lagrangian float whose empirical tilt response suggests partial resonance at short wave periods. Using realistic wind–wave spectra, we quantify the resulting biases and find typical magnitudes of several centimeters per second for horizontal velocities and several millimeters per second for vertical velocities under open-ocean conditions. Because wave-induced biases depend strongly on platform configuration, we provide an analytical framework and numerical tools to assess biases for individual platforms and deployments.

SIGNIFICANCE STATEMENT: Autonomous ocean platforms commonly use acoustic Doppler current profilers (ADCPs) to measure currents, but surface waves can induce platform motions that affect these measurements. This study shows that partially resonant, phase-lagged platform motion – expected for most real-world systems – can introduce systematic biases in velocity estimates, including the biases in the vertical component that have not been previously identified. We present a general analytical framework that accounts for platform dynamics, wave conditions, and instrument geometry and enables deployment-specific bias assessment and mitigation. These results are directly relevant to the interpretation of ADCP observations from autonomous platforms and inform the design of future observing systems targeting weak vertical motions in the ocean.

1. Introduction

Compact autonomous marine vehicles, both surface and submersible, are now commonly used to conduct observations of ocean velocities using acoustic Doppler current profilers (ADCPs). However, in the inevitable presence of surface waves, ADCP measurements conducted by these platforms are susceptible to biases stemming from wave-coherent orbital motion and platform tilting. Our previous paper on this subject (Shcherbina and D'Asaro 2025, hereafter SD25) derived analytical expressions and numerical estimates of wave-induced biases across a range of scenarios. Among these, two limiting cases of platform tilt response to wave forcing were examined: a hydrostatic response, in which the platform instantaneously aligns with the local antigravity direction, and an inertial response, in which it aligns with the vertical material-line vector.

Real-world sampling platforms can exhibit more complex behavior than either idealized limit. In particular, some degree of resonant response may occur, producing both an increase in the platform tilt amplitude and a phase shift relative to the wave forcing. It can be anticipated that the amplitudes and vertical structure of wave-induced biases would be altered in this case. As will be shown in this paper, *vertical* velocity bias can arise in addition to the horizontal velocity biases considered in previous studies.

D'Asaro and Shcherbina (2026, hereafter DS26) investigated the actual response of an APL Lagrangian Float (MLF) using data from multiple deployments under a range of wave conditions. The float was found to exhibit partial resonance at a wave period of approximately 3 s. A full response model for wave periods from 2 to 20 s was also developed. In this paper, we evaluate the wave-induced biases associated with the specific response function of the MLF.

In section 2, we briefly revisit the analytical and numerical frameworks used in our analysis. Section 3 then examines wave-induced platform tilt, including the phase-lagged resonant response, and the resulting motion of the ADCP sampling volume. In Section 4, we derive analytical expressions for wave-induced biases in the general partially resonant case and show how a phase-lagged tilt response leads to vertical velocity bias. Section 5 explores alternative vertical-velocity reconstruction methods that reduce the overall bias. In Section 6, we apply this framework to quantify wave-induced biases in ADCP measurements from a specific Lagrangian float. The main findings are summarized and discussed in Section 7.

2. Methods

a. Analytical framework

We start with a short recap of the analytical framework developed in SD25; readers are referred there for a more complete treatment. As before, we consider a quasi-Lagrangian platform conducting velocity measurements in the presence of surface gravity waves. For simplicity, we postulate a monochromatic deep-water linear wave with the amplitude a, wavenumber k, and cyclic frequency ω propagating in the x direction. Its surface elevation is given by

$$\eta = a \sin\phi, \tag{1}$$

where $\phi = kx - \omega t$ is the wave phase. The wave amplitude a is small compared to the wavelength, so that the wave steepness parameter $(ak) \ll 1$. We express coordinates in the $x-z$ plane using complex notation, $X = x + iz$. With this notation, orbital motion of a fluid particle can be expressed as

$$X = X_0 + X_0' = X_0 + ae^{i(kx_0 - \omega t) + kz_0} = X_0 + ae^{i\phi_0 + kz_0}, \tag{2}$$

where $X_0 = x_0 + iz_0$ is the mean particle position. The corresponding wave velocity field, in complex notation, $U_0 = u_0 + iw_0$, is given by

$$U = -ia\omega e^{i(kx_0 - \omega t) + kz_0} = -ia\omega e^{i\phi_0 + kz_0}. \tag{3}$$

As shown in SD25, linearized expression for the velocity sampled along an arbitrary measurement volume trajectory $X_m(t)$ can be expressed as

$$U_m \equiv U(X_m, t) \approx U_1 + \omega k X_1^{'} X_m^{'*}, \tag{4}$$

where $U_1 = U(X_1, t)$ is the "true" Eulerian velocity at the nominal measurement location X_1, and $X_m^{'} = X_m - X_1$ are the wave-induced perturbations of the sampling location. When this motion of sampling volume $X_m^{'}$ is partially coherent with the wave orbital motions $X_1^{'}$, the quadratic term $X_1^{'} X_m^{'*}$ contains a non-periodic component. This non-periodic component is the origin of the wave-induced bias in the measured velocity.

In section 3 we will discuss the measurement volume trajectories resulting from resonant wave-induced tilting of the float. In section 4 we will derive corresponding analytic expressions for the ensuing biases in horizontal and vertical velocity measurements.

b. Semi-analytical model

As in SD25, we will also use a semi-analytical model to validate and extend the analytical expressions for the wave-induced biases. Platform motion is simulated according to (2), and the platform tilt is modeled based on the wave properties and a specified platform response function (see section 3). The velocity field is then sampled with multiple "beams" and "cells," and processed as it would be with an ADCP.

This model is semi-analytical, in the sense that the platform trajectory and velocity sampling are computed analytically, while the subsequent averaging is numerical. Unlike the analytical framework, the model does not rely on a linearized expansion of the velocity field (4) and can therefore handle larger excursions of the sampling volume. Similarly, it does not require a small-angle approximation for platform tilt (see section 3) and can therefore handle arbitrary wave-induced variations in platform orientation.

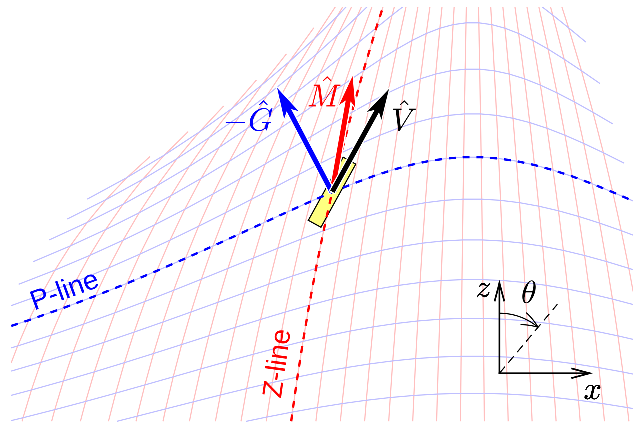

FIG. 1. Orientation of a sampling platform (yellow rectangle) in a wave-induced deformation field (the wave steepness is exaggerated). Material fluid P- and Z-lines are shown in blue and red, respectively, along with their orientation vectors $-\hat{G}$ ("anti-gravity) and $\hat{M}$. Orientation of the platform "mast" vector $\hat{V}$ is determined by the platform dynamics and may not align with either $-\hat{G}$ or $\hat{M}$. The conventions for axes and tilt angles are illustrated in the bottom-right corner.

3. Wave-induced platform tilt

a. Wave deformation field

In a monochromatic wave field, the deformation and tilt of fluid elements can be described using two complementary material lines (Fig. 1). The "P-line" is an isopotential line (actually, a surface in 3D) that would be horizontal in absence of waves. This line is tangent to the local instantaneous fluid velocity, and perpendicular to the local effective gravity vector G. In contrast, the "Z-line" is a material fluid line that would be vertical in absence of waves. As waves propagate, this line deforms under the action of the velocity field. To characterize local tilting of the two lines, we will use the "anti-gravity" vector $-G$ pointing normal to the P-line, and the vector M pointing upwards along the Z-line. In the absence of waves, the two vectors coincide with the upward unit vector $\hat{Z} = i$. Under wave motion, they oscillate symmetrically relative to the vertical, reflecting the tilting and deformation of the fluid elements.

Using the wave kinematics equations, the two vectors can be expressed as

$$M = i + ake^{i\phi_0 + kz_0}, \tag{5}$$

$$-G = i - ake^{i\phi_0 + kz_0}. \tag{6}$$

Note that these vectors are not normalized. Using the small-angle approximation ($ak \ll 1$), we can obtain corresponding unit vectors

$$\hat{M} = i + \Re[ake^{i\phi_0 + kz_0}], \tag{7}$$

$$-\hat{G} = i + \Re[-ake^{i\phi_0 + kz_0}], \tag{8}$$

where $\Re[]$ is the real part operator (see SD25 for details). These vectors can also be expressed in terms of tilt angles,

$$\hat{M} = i + \theta_Z, \tag{9}$$

$$-\hat{G} = i + \theta_G, \tag{10}$$

where $\theta_Z = \Re[ake^{i\phi_0 + kz_0}]$ and $\theta_G = \Re[-ake^{i\phi_0 + kz_0}] = -\theta_Z$ are the material line tilt angles, as in DS26. We deliberately delay application of the real part operator to emphasize that $\pm ake^{(i\phi_0 + kz_0)}$ is the analytic representation of the tilt angles – which would be useful in discussion of spectral transfer functions below.

b. Platform response

As in SD25, we assume that, to the first order, the platform follows the wave orbital motion of the water parcels. For neutrally-buoyant and profiling floats, this approximation is supported by observations for a wider range of wave spectrum (D'Asaro 2003). The tilt of the platform is governed by a balance of hydrostatic and hydrodynamic torques, as discussed in detail in DS26. Depending on the geometric shape of the platform and its hydrostatic stability, a platform would generally exhibit a frequency-dependent tilt response that can be characterized using a general relationship

$$\hat{V} = i + \theta = i + \Re[\gamma ake^{i\phi_0 + kz_0}] \tag{11}$$

where γ is a complex frequency-dependent response factor. As discussed in SD25, $\gamma = -1$ corresponds to hydrostatic response mode ($\hat{V} = -\hat{G}$), and $\gamma = 1$ corresponds to inertial response ($\hat{V} = \hat{M}$). More generally, γ can be seen as a spectral transfer function between the platform tilt angle θ and the tilt of the Z-line θ_Z, $T_{\theta Z}(\omega)$ in DS26 notation. Note that since θ_z and θ_G are 180° out of phase,

$$\gamma = T_{\theta Z} = -T_{\theta G}. \tag{12}$$

It is important to note that the transfer function is applied to the analytic representation of the tilt angles *before* the real part is taken. This approach allows for arbitrary phase shifts between the forcing and the response (naturally, this is only relevant for complex-valued transfer functions).

DS26 investigated the response function $T_{\theta G}$ of a Lagrangian Float and developed an empirical model

$$T_{\theta G}(\omega) = \frac{\sigma^2 - i\kappa\omega}{\sigma^2 - \omega^2 - iq\omega}, \tag{13}$$

where $\sigma = 2.01\, rad\, s^{-1}$ is the resonant angular frequency (corresponding to the cyclic resonant frequency $f = (2\pi)^{-1}\sigma = 0.32\, Hz$, $\kappa = 0.37\, rad\, s^{-1}$ is the shape eccentricity parameter, and $q = 0.88\, rad\, s^{-1}$ is the rotational frictional parameter. The MLF resonant frequency corresponds to the period $f^{-1} = 3.1\, s$ and wavelength of 16 m. Waves of this scale coincide with the peak of a Pierson-Moskowitz fully developed sea spectrum generated by winds of about $U_{10} = 4\, m\, s^{-1}$. Consequently, the MLF resonant response could be expected to be commonly excited during most deployments in typical ocean wave conditions.

The general shape of the spectral response function and the temporal behavior of the resonant tilt response are illustrated in Fig. 2. At low frequencies, the float response is in-phase with the forcing with $T_{\theta G}$ real and approaching 1 (corresponding to $\gamma \approx -1$). This behavior reflects the platform aligning with the effective gravity, as expected for any platform with strong hydrostatic restoring moment (i.e., $\sigma \gg \omega$, $\sigma \gg \kappa$), which is the reason this response is called 'hydrostatic' (Longuet-Higgins 1986). Conversely, for a platform with a weak righting moment ($\sigma \ll \omega$, $\sigma \ll \kappa$), the response function would asymptote to $T_{\theta G}(0) = q^{-1}\kappa = -\lambda$, where λ is the Jeffery shape eccentricity parameter (Jeffery 1922; Bretherton 1962). This case corresponds to the classical Jeffery-type alignment with the principal strain direction – which can have characteristics

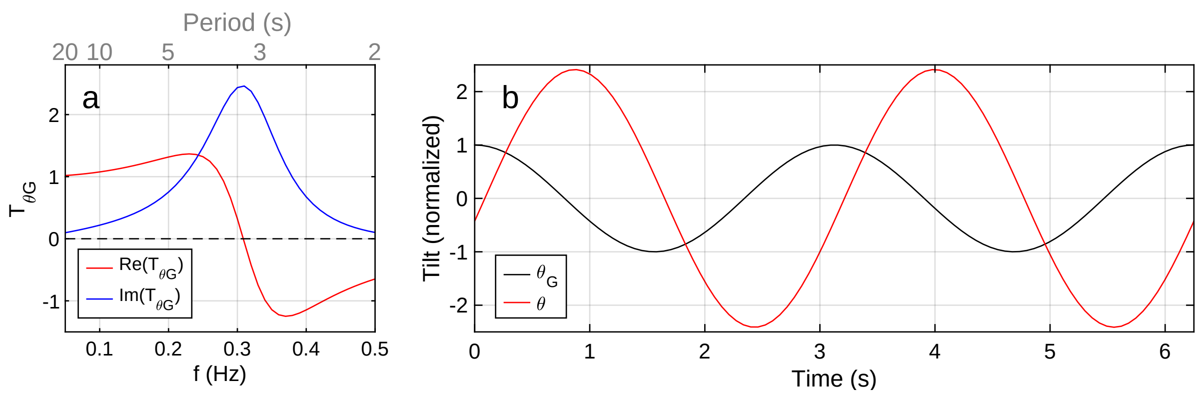

FIG. 2. Empirical model of Lagrangian Float tilt response based on DS26. a) Empirical spectral transfer function from the effective gravity tilt angle θ_G to the tilt of the float θ as a function of wave frequency. b) Time series of the forcing (θ_G, black) and the float response (θ, red) tilt angles at resonant frequency f=0.32 Hz; tilt angles are normalized by θ_G amplitude, ake^{kz_0}. Note the $\pi/2$ phase lag and significant amplification of the response, both hallmarks of resonance.

of either inertial ($\gamma = \lambda > 0$) or hydrostatic ($\gamma = \lambda < 0$) response[1]. Thus, the purely real-valued response considered in SD25 is applicable in the low-frequency limit, where either the hydrostatic (strong-restoring) or Jeffery (weak-restoring) asymptotes govern the tilt dynamics

At high frequencies, $T_{\theta G}$ is also real but negative (corresponding to $0 < \gamma < 1$), so the platform tilt is out of phase with the effective gravity tilt θ_G (but in-phase with $\theta_Z = -\theta_G$). Such behavior is universal among systems with finite inertia and corresponds to the attenuated inertial-response regime. SD25 formulae would be applicable in this regime as well.

At intermediate frequencies, particularly near the 0.32 Hz resonance, the response is amplified ($|T_{\theta G}|$ reaching 2.5) and increasingly lagging the forcing. The strong imaginary component of $T_{\theta G}$ observed over the broad range of frequencies requires us to extend the wave-induced bias analysis of SD25 to complex values of response parameter $\gamma = -T_{\theta G}$. As will be shown below, this extension is not as trivial as substituting a complex γ into the SD25 formulae.

c. *Phase-lagged sampling volume trajectories*

As described in detail in SD25, deriving the wave-induced bias formulae begins with determining the trajectories of the ADCP sampling volumes, $X_m(t)$. Wave-induced biases arise from the phase-

[1]Note that although a flat disc ($\lambda = -1$) exhibits a hydrostatic-like response ($T_{\theta G} \approx 1$), its alignment in this case would be governed by strain-induced Jeffery alignment rather than hydrostatic forces.

locked relationships between these trajectories and the wave orbital velocities (see SD25, section 3a). We only need to reconsider the biases arising from the platform tilt – i.e., the "sweep" and frame rotation biases, plus the associated ADCP beam effects.

Consider a sampling volume at a nominal (vector) offset D from the platform, so that the nominal location of this volume is $X_1 = X_0 + D$. For a pair of symmetric ADCP beams,

$$D^{\pm} = r(i \pm \tan\beta) = ir(\cos\beta)^{-1} e^{\mp i\beta}, \tag{14}$$

where r is the nominal vertical distance to the sampling volume (positive for upward-looking instrument), and β is the ADCP beam angle. For a hypothetical "vector" sampler that measures the full velocity vector at a remote location (as considered in SD25), the displacement vector D takes the simple form $D = ir$. The sampling volume trajectories around their nominal positions are the superposition of the platform's orbital motion (X_0') and the sweeping motion (X_t') produced by time-varying platform tilt,

$$X_m' = X_0' + X_t'. \tag{15}$$

As in SD25, the platform motion is described as

$$X_0' = ae(i\phi_0 + kz_0), \tag{16}$$

and the sweeping term is given by

$$X_t' = -i\hat{V}D - D = -D(1 + i\hat{V}), \tag{17}$$

where $\hat{V}$ is the varying platform "mast" orientation unit vector. As expected, X_t' vanishes for an upright platform, $\hat{V} = i$. As discussed above, the platform tilt response can be described as

$$\hat{V} = i + \Re[\gamma ake^{i\phi_0 + kz_0}] = i + ake^{kz_0}(\gamma_r \cos\phi_0 - \gamma_i \sin\phi_0), \tag{18}$$

where $\gamma = \gamma_r + i\gamma_i$ is a complex frequency-dependent response factor (transfer function). This leads to the following linearized expression for the sweeping motion of the sampling volumes of the two

ADCP beams:

$$X_t'^{\pm} = -D^{\pm}(1 + i\hat{V}) = akre^{kz_0}(\cos\beta)^{-1}e^{\mp i\beta}(\gamma_r\cos\phi_0 - \gamma_i\sin\phi_0). \tag{19}$$

Imaginary component of the response function, γ_i, produces a phase shift between the orbital and sweeping motions of the sampling volumes. As a result, the sampling volume trajectories are skewed and rotated (Fig. 3a) compared to the real-valued response parameter cases (Fig. 3b,c). There is also a notable difference between the two ADCP beams.

At this point we can already anticipate that, unlike the cases considered in SD25, the wave-induced biases arising from the resonant (phase-lagged) tilt response of the measuring platform would involve both the horizontal and the vertical components of measured velocities.

4. Wave-induced biases

Each of the two wave-induced time-varying terms in (15) gives rise to a bias in measured phase-averaged velocities. An additional frame-rotation bias arises if the instrument is not "aware" of its true wave-induced tilt and therefore conducts averaging in its own frame of reference. To first order, these biases are additive and independent, allowing us to compute them separately. While these biases correspond directly to those considered in SD25, the resulting analytical expressions are critically different for the resonant tilt response considered here due to the imaginary component of the response function.

a. Platform motion bias

The platform motion bias arises from the $X_0' = ae^{i\phi_0 + kz_0}$ component of sampling volume motion. This bias is independent of the platform tilt, therefore SD25 expression for the velocity bias still holds:

$$U_{wr} = U_{S0}e^{kz_0}(R_u e^{kz_1} - e^{kz_0}). \tag{20}$$

Here, $U_{S0} = a^2\omega k$ is the surface Stokes drift which serves as a common scaling factor, and

$$R_u = \frac{\sin(\beta + kr\tan\beta)}{\sin\beta} \tag{21}$$

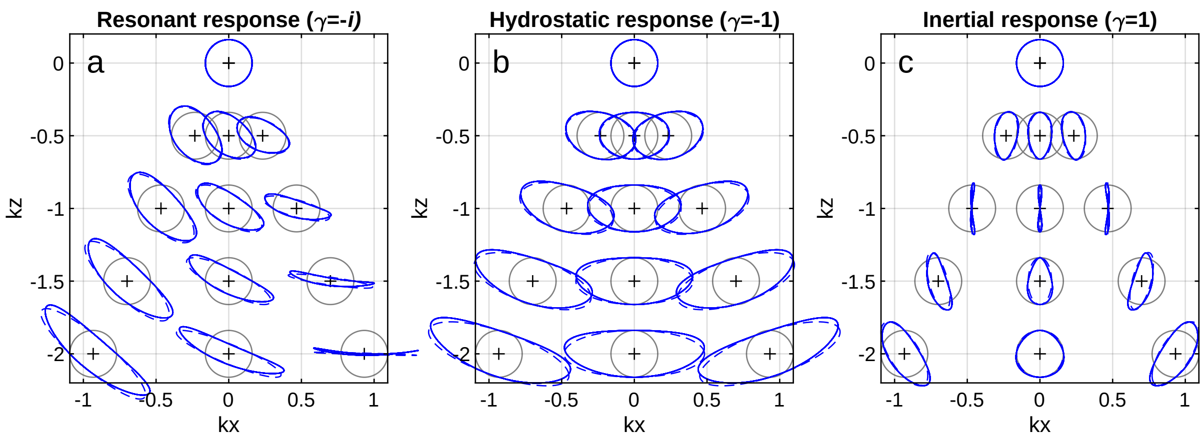

FIG. 3. (a) Wave-induced trajectories of ADCP sampling volumes for resonant platform tilt model ($\gamma = -i$), compared to (b) hydrostatic ($\gamma = -1$), and (c) inertial ($\gamma = 1$) responses. Trajectories obtained from a semianalytical model are shown in blue solid lines, with the linearized approximations shown with dashed lines. Trajectories in the absence of platform tilt are shown in grey for reference. ADCP beam angle $\beta = 25^\circ$ assumed.

is the horizontal velocity response function associated with ADCP measurements, which are derived from the radial velocities along two beams inclined at $\pm\beta$ (see SD25 for details). The associated vertical velocity response function

$$R_w = \frac{\cos(\beta + kr\tan\beta)}{\cos\beta} \tag{22}$$

does not enter this expression but will become important later.

b. Sweeping bias

The sweeping bias arises from the X_t' component of sampling volume motion. Eulerian velocities along the sweeping trajectories are computed using the linearized expression

$$U_t^{\pm} = U_1^{\pm} + \omega k X_1' \, X_t'^{\pm *} = U_1^{\pm} + a\omega k e^{i\phi_1^{\pm} + kz_1} \cdot r(\cos\beta)^{-1} e^{\pm i\beta} a k e^{kz_0} (\gamma_r \cos\phi_0 - \gamma_i \sin\phi_0) = U_1^{\pm} + U_{S0} e^{k(z_0+z_1)} kr(\cos\beta)^{-1} e^{i(\phi_1^{\pm} \pm \beta)} (\gamma_r \cos\phi_0 - \gamma_i \sin\phi_0) \tag{23}$$

Averaging over the wave phase eliminates harmonic terms, producing

$$\bar{U_t^{\pm}} = U_{S0} e^{k(z_0+z_1)} kr(\cos\beta)^{-1} e^{\mp\beta} \langle e^{i\phi_1^{\pm}} (\gamma_r \cos\phi_0 - \gamma_i \sin\phi_0) \rangle \tag{24}$$

The wave phase variation associated with the ADCP beam separation is

$$\phi_1^{\pm} = \phi_0 \pm kr\tan\beta = \phi_0 \pm \phi', \tag{25}$$

where $\phi' = kr\tan\beta$ is half the wave phase difference between the two beams. Therefore,

$$\bar{U_t^{\pm}} = U_{S0} e^{k(z_0+z_1)} kr(\cos\beta)^{-1} e^{\pm i(\beta+\phi')} e^{i\phi_0} (\gamma_r \cos\phi_0 - \gamma_i \sin\phi_0) = \frac{1}{2}(\gamma_r - i\gamma_i) U_{S0} e^{k(z0+z1)} kr(\cos\beta)^{-1} e^{\pm i(\beta+\phi')}. \tag{26}$$

ADCP records the along-beam components of actual velocities,

$$\bar{B^{\pm}} = \Im[\bar{U_t^{\pm}} e^{\pm i\beta}], \tag{27}$$

where $\Im[\cdot]$ is the imaginary part operator. Expanding it, we obtain

$$\bar{B^{\pm}} = \frac{1}{2} U_{S0} e^{k(z_0+z_1)} kr(\cos\beta)^{-1} \; \Im[(\gamma_r - i\gamma_i) e^{\pm i(2\beta+\phi')}] \quad \frac{1}{2} U_{S0} e^{k(z_0+z_1)} kr(\cos\beta)^{-1} (\pm\gamma_r \sin(2\beta+\phi') - \gamma_i \cos(2\beta+\phi')), \tag{28}$$

Following the standard ADCP processing procedure, we reconstruct the full velocity vector from the beam velocities:

$$U_t = \frac{\bar{B^+} - \bar{B^-}}{2\sin\beta} + i\frac{\bar{B^+} + \bar{B^-}}{2\cos\beta} = \frac{1}{2} U_{S0} e^{k(z_0+z_1)} kr[\gamma_r \frac{\sin(2\beta+\phi')}{\sin 2\beta} - i\gamma_i \frac{\cos(2\beta+\phi')}{1+\cos 2\beta}]. \tag{29}$$

Comparing this with the corresponding expression in SD25 (eq. 60), we see that the imaginary part of the response function, γ_i, gives rise to a sweeping bias in the *vertical* velocity estimate, in addition to the horizontal velocity bias examined previously. This expression can also be re-written as

$$U_t = \frac{1}{2}(\gamma_r R_{ut} - i\gamma_i R_{wt}) kr U_{S0} e^{k(z_0+z_1)} \tag{30}$$

using modified ADCP sweeping response functions

$$R_{ut} = \frac{2\sin(2\beta+\phi')}{\sin 2\beta} = \frac{2\sin(2\beta+kr\tan\beta)}{\sin 2\beta}, \tag{31}$$

$$R_{wt} = \frac{2\cos(2\beta+\phi')}{1+\cos 2\beta} = \frac{2\cos(2\beta+kr\tan\beta)}{1+\cos 2\beta}. \tag{32}$$

c. Frame rotation bias

Next, we examine the frame rotation bias arising if the velocity averaging is carried out in the ADCP frame of reference. It should be reminded that this bias can, in principle, be eliminated by rotating each ping's velocity measurements to Earth coordinates prior to averaging, but doing so requires accurate attitude measurements. As discussed in DS26, accurately measuring platform attitude in the wave band is not an easy task even with the dedicated inertial sensors. Consequently, the frame rotation bias needs to be quantified. In the nominally-upright instrument frame of reference, measured relative velocities are recorded as

$$U_{1i} = (U_1 - U_0)(i\hat{V}^*), \tag{33}$$

where the multiplier $i\hat{V}^* = 1 + iake^{kz_0}(\gamma_r\cos\phi_0 - \gamma_i\sin\phi_0)$ represents the rotation from Earth to instrument frame. Applying phase averaging, we obtain

$$\overline{U_{1i}} = \langle (U_1 - U_0)iV^* \rangle = -ia\omega\langle (e^{kz_1+i\phi_0} - e^{kz_0+i\phi_0})(1 + iake^{kz_0}(\gamma_r\cos\phi_0 - \gamma_i\sin\phi_0))\rangle = \frac{1}{2}U_{S0}e^{kz_0}\left((\gamma_r - i\gamma_i)e^{kz_1} - (\gamma_r - i\gamma_i)e^{kz_0}\right). \tag{34}$$

To obtain the final expression for the frame rotation bias, we need to apply the ADCP transfer functions to both components of the averaged ambient velocity $\langle U_1 i\hat{V}^* \rangle$ — but, importantly, not to the averaged platform motion $\langle U_0 i\hat{V}^* \rangle$, which is unaffected by ADCP measurement artifacts:

$$U_f = \frac{1}{2}U_{S0}e^{kz_0}((\gamma_r R_u - i\gamma_i R_w)e^{kz_1} - (\gamma_r - i\gamma_i)e^{kz_0}). \tag{35}$$

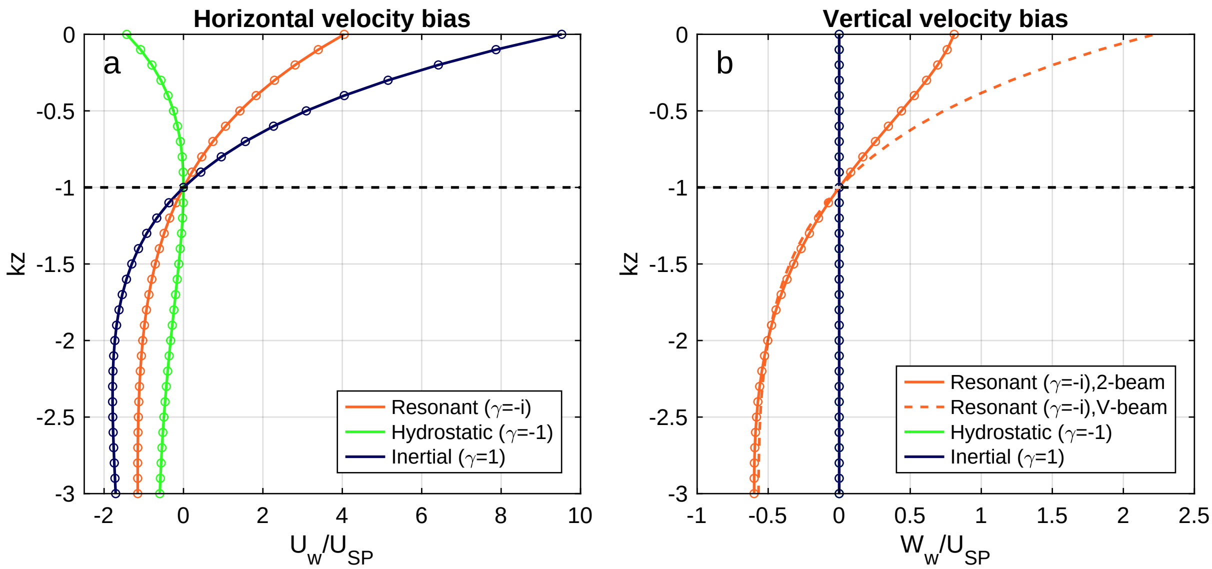

FIG. 4. Wave-induced tilt and motion biases in (a) relative horizontal and (b) vertical velocities measured by a up- and downward-looking ADCPs mounted on a subsurface quasi-Lagrangian platform with resonant ($\gamma = -i$), hydrostatic ($\gamma = -1$), and inertial ($\gamma = 1$) responses. Analytical estimates are shown in solid lines, overlayed with the semianalytical simulation results (circles). Dashed orange line in (b) shows the vertical beam bias for the resonant case. Horizontal dashed line marks the platform depth (set to $z_0 = k^{-1}$ in this example). Velocity bias values are normalized by the Stokes drift at the level of the platform, U_{SP}; the depth is normalized by the inverse wavenumber k^{-1}. Note the difference in the velocity axis scales.

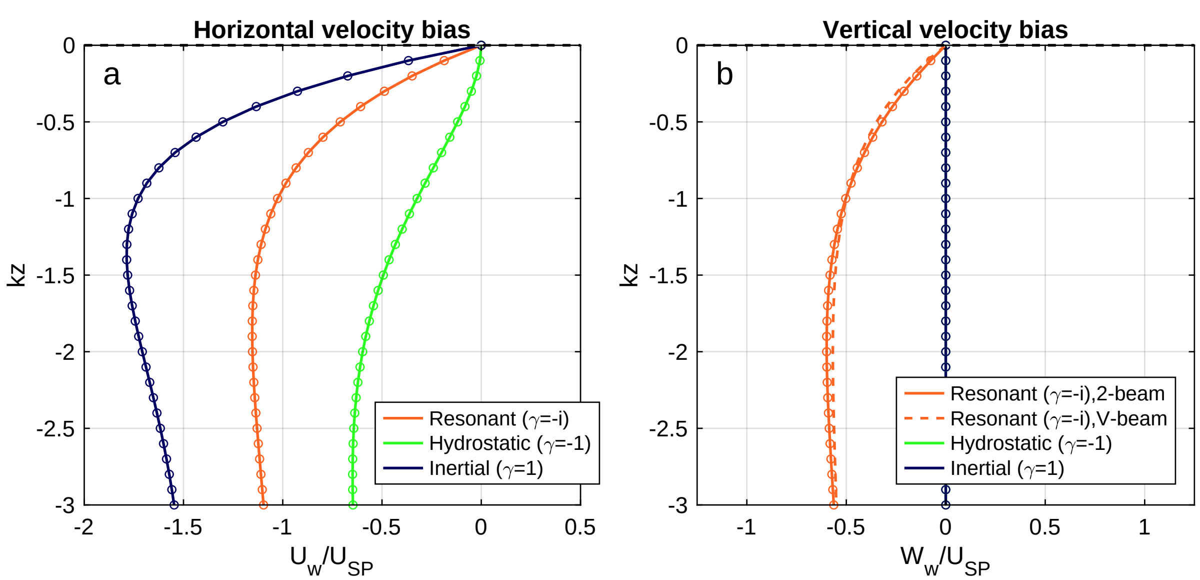

FIG. 5. Same as Fig. 4, but for a surface platform equipped with a downward ADCP.

d. Net wave-induced bias

Net relative wave induced bias is obtained by adding the expressions for motion (20), sweeping (30), and frame-rotation biases (35). For insight into the structure of the resulting bias profiles, it is convenient to express them in terms of platform depth z_0 and measurement range $r = z_1 - z_0$. We also present horizontal and vertical velocity biases separately for clarity:

$$u_w = \left((R_u + \tfrac{1}{2}\gamma_r (R_u + krR_{ut}))e^{kr} - (\tfrac{1}{2}\gamma_r + 1) \right) U_{SP}, \tag{36}$$

$$w_w = -\tfrac{1}{2}\gamma_i \left((R_w + krR_{wt})e^{kr} - 1 \right) U_{SP}, \tag{37}$$

where

$$U_{SP} = U_{S0} e^{2kz_0} = a^2 \omega k e^{2kz_0} \tag{38}$$

is the Stokes drift at the platform depth that serves as the bias amplitude scaling parameter. In this form, it is easy to see that for a platform at fixed depth U_{SP} is also constant, and therefore bias profiles depend only on the scaled measurement range kr. Equations (36-37) imply that surface and sub-surface platforms share the same relative bias profiles, but the bias magnitudes for a subsurface platform are much smaller for the same range and wave forcing because of the rapid decay of the e^{2kz_0} factor with platform depth. Examples of normalized net wave-induced bias profiles for ADCPs mounted on a sub-surface and surface platforms with different response characteristics are shown in Fig. 4 and Fig. 5. Analytical expressions are in good agreement with the semi-analytical model results.

As expected, the resonant horizontal velocity bias ($\gamma = -i$) is intermediate between the hydrostatic ($\gamma = -1$) and inertial ($\gamma = 1$) response limits, reflecting the consistent effect of the real part of the response function on the wave-induced bias (36). In contrast, a resonant (and, more generally, any phase-lagged) response with $\gamma_i \neq 0$ introduces a substantial vertical velocity bias that is not present in hydrostatic or inertial response cases.

All biases vanish as $kr \to 0$, and most change sign between upward- and downward-looking orientations; the horizontal bias for the hydrostatic response case ($\gamma_r = -1$) is an exception, as it stays negative. For an upward-looking ADCP ($kr > 0$) the bias is dominated by the sweeping term, whose magnitude increases rapidly with range following the $\sim kre^{kr}$ asymptotic. Presence of the periodic slant-beam transfer functions (Fig. 6), however, makes the biases oscillatory. Horizontal and vertical biases first change signs in the vicinity of the first zeros of R_{ut} and R_{wt}, occurring at $kr \approx 4.9$ and 1.5, respectively. For a downward-looking ADCP, the biases are dominated by the frame rotation effects and the platform's own motion, to which the velocity measurements are referenced. They approach finite limits as $kr \to -\infty$,

$$u_w^{-\infty} = -(\tfrac{1}{2}\gamma_r + 1)U_{SP}, \tag{39}$$

$$w_w^{-\infty} = -\tfrac{1}{2}\gamma_i U_{SP}. \tag{40}$$

As a result, downward-looking configurations typically exhibit a weak mid-range maximum in biases at a range of about $kr \sim 1 - 2$. Although the slant-beam transfer functions cause bias oscillations, their amplitudes decay rapidly and therefore not likely to be important.

Horizontal and vertical velocity biases generally scale with the real and imaginary parts of the response factor γ, respectively. Near the resonance frequency, both the real and (especially) the imaginary components of the response function can exceed unity in magnitude (e.g., see Fig. 2). In such cases, the wave-induced biases will be correspondingly amplified.

e. ADCP beam alignment

In the preceding derivations, we assumed that the ADCP beam pair was aligned with the wave propagation direction, an assumption that is seldom satisfied in real life observations. At first glance, one might expect the wave-induced biases to be a simple projection of the down-wave biases onto the plane of the ADCP beam pair. In practice, the situation is considerably more complex.

When the ADCP beam-pair axis is rotated by an angle α relative to the wave propagation direction, several aspects of the wave-beam interaction are modified simultaneously. The most direct effect is a reduction of the horizontal component of the wave orbital velocity "seen" by the beams, scaling as $\cos\alpha$. Additionally, the projection of the beam spread onto the $x - z$ plane is reduced, producing a smaller effective beam angle $\beta_x = \tan^{-1}(\cos\alpha \tan\beta)$. This reduction decreases the wave phase difference between the two slanted ADCP beams, which, in turn can be expected to reduce the effects of the beam geometry. Moreover, the wave-induced sweeping trajectories of the sampling volumes are affected by misalignment because these also depend on the projected beam angle.

Together, these effects modify wave-induced biases in a non-trivial manner. Platform motion:

$$U_{wr}^{\alpha} = U_{S0}e^{kz_0}(R_u^{\alpha}e^{kz_1} - \cos\alpha e^{kz_0}). \tag{41}$$

Sweeping:

$$U_t^{\alpha} = \tfrac{1}{2}krU_{S0}e^{k(z_0+z_1)}(\gamma_r R_{ut}^{\alpha} - i\gamma_i R_{wt}^{\alpha}). \tag{42}$$

Frame rotation:

$$U_f^{\alpha} = \tfrac{1}{2}U_{S0}e^{kz_0}((\gamma_r R_u^{\alpha} - i\gamma_i R_w^{\alpha})e^{kz_1} - (\gamma_r\cos\alpha - i\gamma_i)e^{kz_0}). \tag{43}$$

Most of the alignment effects are captured by the modified ADCP beam response functions:

$$R_u^{\alpha} = \frac{\cos\beta\sin(\phi_x') + \cos\alpha\sin\beta\cos(\phi_x')}{\sin\beta}, \tag{44}$$

$$R_w^{\alpha} = \frac{\cos\beta\cos(\phi_x') - \cos\alpha\sin\beta\sin(\phi_x')}{\cos\beta}, \tag{45}$$

where $\phi_x' = kr\tan\beta_x = kr\cos\alpha\tan\beta$. Similarly, the sweeping response functions become

$$R_{ut}^{\alpha} = \frac{\cos\beta\sin(\beta_x + \phi_x') + \cos\alpha\sin\beta\cos(\beta_x + \phi_x')}{\sin\beta\cos\beta_x}, \tag{46}$$

$$R_{wt}^{\alpha} = \frac{\cos\beta\cos(\beta_x + \phi_x') - \cos\alpha\sin\beta\sin(\beta_x + \phi_x')}{\cos\beta\cos\beta_x}. \tag{47}$$

Derivation of these expressions is given in the Appendix A. For the aligned ADCP case ($\alpha = 0$, $\beta_x = \beta$), these reduce to (21)-(22) and (31)-(32). In general, both the horizontal and vertical velocity response functions vary with the misalignment angle α as shown in Fig. 6. All response functions are periodic in kr with the period $2\pi/\tan\beta_x$. As α increases, the oscillation period increases accordingly. In the limiting case of the beam pair oriented perpendicular to the wave propagation direction ($\alpha = \frac{\pi}{2}$), the response functions reduce to constants: $R_u = R_{ut} = 0$ and $R_w = R_{wt} = 1$. Thus, the horizontal velocity biases vanish while the vertical velocity biases remain finite (as long as $\gamma_i \neq 0$) but unaffected by the beam spread.

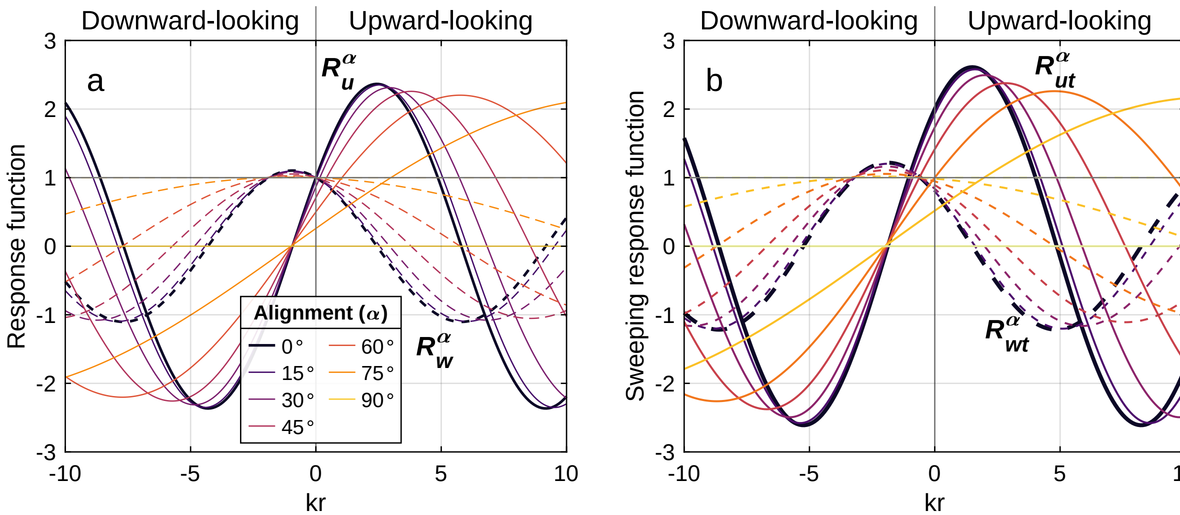

317 Fig. 6. (a) ADCP response functions and (b) sweeping response functions for horizontal (solid lines) and vertical (dashed lines) velocities as a function of ADCP alignment angle α. Bold lines correspond to aligned ADCP case ($\alpha = 0$), as considered in SD25. ADCP beam angle of 25° is used.

f. Vertical beam considerations

Several modern ADCPs, such as the Nortek Signature series and Teledyne RDI Sentinel V, can be equipped with a vertical (fifth) beam in addition to the standard slanted beams. In principle, this vertical beam enables direct line-of-sight measurements of vertical velocity because it does not rely on the multi-beam geometric reconstruction used by conventional ADCP configurations (Shcherbina et al. 2018; Comby et al. 2022). In other words, the vertical velocity response function for the V-beam is always unity, $R_w^V = R_{wt}^V = 1$.

When it comes to wave-induced vertical velocity biases, the advantages of the dedicated V-beam are less straightforward. Using (30) and (35), and assuming unity ADCP response functions, the V-beam vertical velocity biases can be obtained as

$$w_{Vt} = -\tfrac{1}{2}\gamma_i kr U_{S0} e^{k(z_0+z_1)}, \tag{48}$$

$$w_{Vf} = -\tfrac{1}{2}\gamma_i U_{S0} e^{kz_0}(e^{kz_1} - e^{kz_0}). \tag{49}$$

For a downward-looking configuration, the V-beam exhibits nearly the same bias as the conventional two-beam reconstruction of vertical velocity (Fig. 5b). This occurs because the two-beam ADCP response functions R_w and R_{wt} are already near unity across the relevant downward-looking ranges (dashed lines in Fig. 6). In a 25° ADCP shown, the departure of the response function from unity remains small $|R_{wt} - 1| < 0.25$ for $-4 \lesssim kr < 0$ (Fig. 6a). Moreover, near $kr \approx -1$, the opposing effects of the ADCP response functions (R_w and R_{wt}) on tilt and sweeping biases nearly cancel, so that the net vertical velocity bias is effectively equivalent to that of the V-beam. For an upward-looking subsurface platform, such as the Lagrangian float, the wave-induced vertical velocity bias in V-beam measurements is substantially larger than that of the conventional two-beam reconstruction Fig. 4). As discussed in SD25, $|R_w| < 1$ for relatively short upward ranges ($0 < kr \lesssim 5$, and so is $|R_{wt}|$ (cf. Fig. 6). Therefore, the ADCP beam reconstruction effect is beneficial: it reduces both the sweeping and frame-rotation biases in measured vertical velocities (in stark contrast to the horizontal biases, see Fig. 12–13 in SD25).

For slanted-beam velocity reconstructions, the frame-rotation biases U_f can be removed by rotating each ping's velocity measurements to Earth coordinates prior to averaging, provided that accurate attitude data are available. For V-beam vertical velocity measurements, however, this approach is not viable: A single beam does not provide the cross-beam velocity components required for such a transformation, and reconstructing them from additional beams would remove the benefits of a single-beam measurement. Frame-rotation bias is therefore appears to be unavoidable in V-beam measurements.

5. Optimal unbiased vertical velocity reconstruction

A five-beam ADCP provides three independent vertical velocity estimates: two reconstructed from the opposing slanted-beam pairs (w_1,w_2), and one measured directly by the vertical beam (w_3). Even more estimates can be obtained by linear combination of these three (e.g., an estimate using all four slanted beams). From the preceding discussion it can be seen that each of these estimates experiences biases due to wave-induced tilt of the platform, but to a different degree.

The biases associated with the slanted-beam reconstructions depend on the alignment of each beam-pair and follow (41)-(43) with two orthogonal angles, α and $\alpha + \frac{\pi}{2}$. In general, both would be affected by the ADCP beam response functions to some extent — except for a beam pair perpendicular to the wave propagation direction. The V-beam biases, given by (48) and (49), do not depend on the ADCP alignment with the waves. It can be seen that the V-beam biases match those of the vertical velocity reconstructed from the cross-wave beam pair ($\alpha = \pi/2$).

It is reasonable to ask whether we can determine which of the three vertical velocity estimates is "better", i.e. least affected by the tilt biases. The three velocity estimates and their biases can be expressed as

$$w_i = w + R_i w_w, \quad i = 1 \ldots 3, \tag{50}$$

where w is the "true" vertical velocity. The bias is expressed as the product of the common bias amplitude w_w and the geometric factors R_i that capture how this bias projects onto each of the three velocity reconstructions. Thus w_w contains all dependence on the wave field and platform response, while the coefficients R_i encode the purely geometric differences among the three ADCP-based reconstructions. As will become apparent later, it is convenient to take the V-beam bias as the bias amplitude, i.e., for the combination of sweeping and frame rotation biases, we set

$$w_w = w_{Vt} + w_{Vf} = -\tfrac{1}{2}\gamma_i \left((1 + kr)e^{kr} - 1 \right) U_{SP}. \tag{51}$$

Then the geometric factors for the two slanted-beam reconstructions are

$$R_i = \frac{(R_w^{\alpha_i} + R_{wt}^{\alpha_i} kr)e^{kr} - 1}{(1 + kr)e^{kr} - 1}, \; i = 1, 2, \tag{52}$$

where α_i is the alignment angle of the two beam-pairs, $\alpha_2 = \alpha_1 + \frac{\pi}{2}$. As discussed in the previous section, the V-beam estimate does not depend on the alignment, so corresponding geometric factor is unity ($R_3 = 1$). Geometric factors can be calculated analytically using the expressions for R_w^{α} and R_{wt}^{α} derived earlier. Despite the presence of exponentials, R_i remain O(1) for both the positive and negative values of kr. Singularity at $kr = 0$ is avoided by continuity extension $R_i|_{kr=0} = 1 - \cos^2\alpha \tan^2\beta$.

If the ADCP orientation angles were known, identifying the "best" estimate would be as trivial as finding the smallest bias scaling factor, $\min|R_i|$ at each range cell. Note that we could make this choice without knowing wave amplitude or platform response characteristics. In a more realistic case where the wave field is poorly known it is impossible to unambiguously determine which of the three biases is smaller. No single estimate is universally superior.

We can, however, exploit the fact that the three reconstructions provide redundant but differently biased estimates of the same quantity, and seek an appropriately weighted recombination

$$\widetilde{w} = \sum_{i=1}^{3} c_i w_i \tag{53}$$

that systematically reduces the biases for an arbitrary ADCP alignment[2]. The choice of the recombination weights c_i depends on the adopted optimality criterion, and the combination can be expected to vary with range. One obvious choice is to seek a linear combination that is unbiased on average over a uniform distribution of unknown alignment angles α from 0 to 2π:

$$\langle \widetilde{w} - w \rangle = 0. \tag{54}$$

Here, angle brackets represent averaging over all possible α. This condition leads to the constraints

$$\sum c_i = 1, \tag{55}$$

$$\sum c_i \bar{R}_i = 0. \tag{56}$$

The two slanted-beam reconstructions differ only by a $\pi/2$ rotation, which implies that $\langle R_1 \rangle = \langle R_2 \rangle = \bar{R}_1$. The average geometric factor $\bar{R}_1$ serves as a measure of the mean (expected value) of the bias in either of the slant-beam reconstructions, normalized by the corresponding bias of the V-beam. Its analytical expression can be obtained from the expressions for R_w^α and R_{wt}^α derived earlier (see Appendix B for details). For the direct vertical-beam estimate, $\langle R_3 \rangle = R_3 = 1$. Because the two slant-beam pairs are symmetric and their orientation relative to the wave direction is unknown, there is no reason to weigh the two slant-beam estimates differently; we therefore set $c_1 = c_2$. Solving the two constraints then gives

$$c_1 = c_2 = \tfrac{1}{2}(1 - \bar{R}_1)^{-1}, \tag{57}$$

$$c_3 = -\bar{R}_1 (1 - \bar{R}_1)^{-1}. \tag{58}$$

[2] Another way to see this recombination as an optimal five-beam vertical velocity reconstruction.

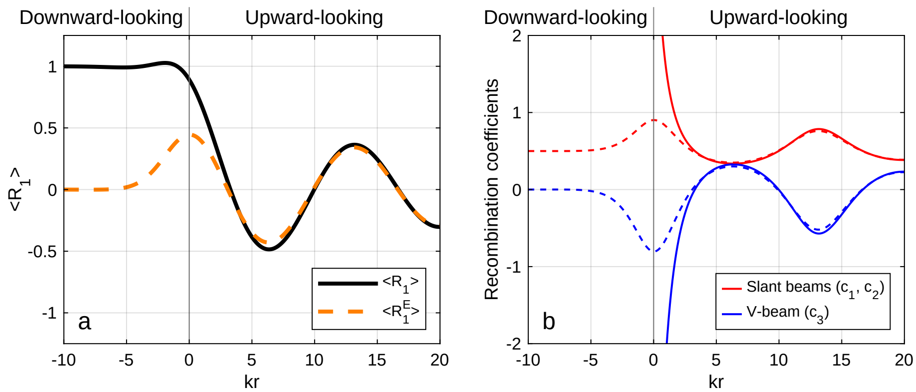

FIG. 7. (a) Mean geometric factor $\bar{R}_1$ describing the relative scaling of vertical-velocity bias in slant-beam reconstruction. (b) Optimal recombination weights for the slant-beam ($c_1 = c_2$, red) and V-beam (c_3, blue) estimates. In both panels, solid curves correspond to the full-bias case (sweeping + frame rotation). Dashed curves show the Earth-frame geometric factor and weights applicable when slant-beam estimates are first rotated into the Earth frame prior to averaging. ADCP beam angle of 25° assumed.

Therefore, the optimal recombination is uniquely determined by the average geometric factor $\bar{R}_1$ which, given a specific ADCP configuration, depends only on the scaled range kr. This dependence for an up-/downward-looking ADCP subject to both sweeping and frame-rotation biases is illustrated in Fig. 7a, along with the corresponding optimal recombination weights (Fig. 7b). Note that the slant-beam contribution to the recombination, $c_1 w_1 + c_2 w_2 = c_1(w_1 + w_2)$, is equivalent to $2c_1 w_4$, i.e. the standard four-beam estimate $w_4 = \frac{1}{2}(w_1 + w_2)$ taken with the weight $2c_1$.

For upward-looking ADCP ($kr > 0$), $\bar{R}_1$ oscillates with the same period as R_w and R_{wt} ($2\pi/\tan\beta$). The oscillation amplitude decays slowly with increasing kr, and $\bar{R}_1$ generally remaining in the [-0.5, 0.5] range. Corresponding optimal recombination weights also oscillate with normalized range and remain O(1). Net-zero bias recombination is therefore feasible in this regime.

Fig. 8 illustrates several examples of unbiased recombination at different normalized ranges. It can be seen that even though the optimal recombination is constrained only to be unbiased *on average*, it tends to have smaller bias than any of the individual estimates at most (though not all!) misalignment angles. Variability of the bias with α is also reduced compared to that of the slant-beam estimates (R_1 and R_2). As expected, the optimal five-beam reconstruction generally outperforms the standard four-beam vertical-velocity estimate , which corresponds to $c_1 = c_2 = 0.5$, $c_3 = 0$ and the bias factor $R_4 = \frac{1}{2}(R_1 + R_2)$ (dashed line).

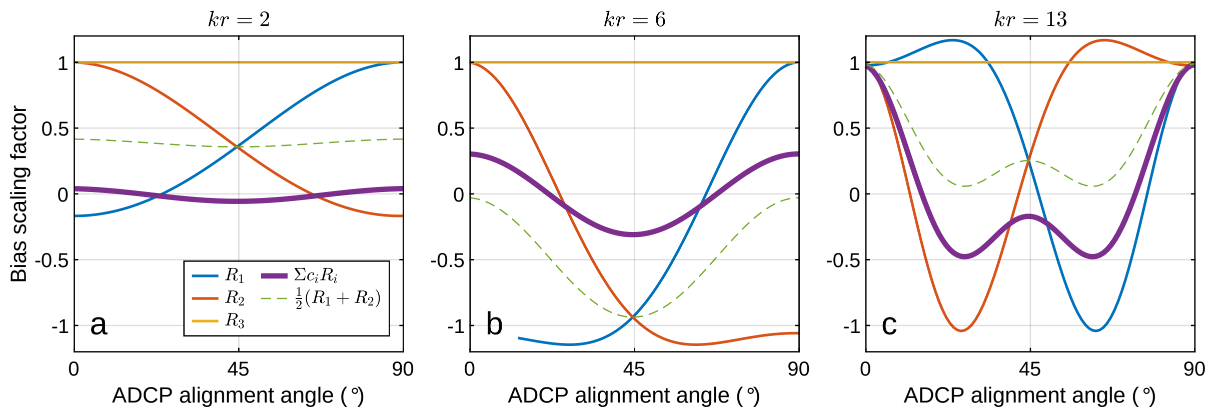

FIG. 8. Examples of optimal unbiased recombination of ADCP vertical velocity estimates for (a) $kr = 2$, (b) $kr = 6$, and (c) $kr = 13$. Bias scaling factors for the two slant-beam reconstructions (R_1, R_2) and the V-beam estimate (R_3) are shown, along with their optimal recombination ($\sum c_i R_i$, thick line). The standard four-beam vertical-velocity estimate bias factor, $R_4 = \frac{1}{2}(R_1 + R_2)$, is included for reference (dashed line).

For downward-looking measurements ($kr < 0$), the behavior is markedly different: $\bar{R}_1$ quickly approaches 1 and then remains nearly constant. This situation ($\bar{R}_1 \approx \bar{R}_3 = 1$) implies that all three reconstructions carry essentially the same bias. This behavior can be understood by examining the structure of the tilt-induced bias: for a downward-looking ADCP ($kr < 0$), the bias is dominated by the frame-rotation distortion of the platform motion, to which the measured beam velocities are referenced. As discussed in section 4c, this component is unaffected by the velocity reconstruction artifacts because if impacts all the beams equally. Therefore, all three vertical velocity reconstructions experience roughly the same bias. Although an optimal solution (57)-(58) formally exists for any $\bar{R}_1 \neq 1$, the corresponding values of the recombination weight become very large when $\bar{R}_1$ is close to unity. Using such weights would drastically amplify noise in the reconstructed velocity.

As discussed earlier, the frame-rotation bias can be removed from the slant-beam reconstructions (but, importantly, not from the V-beam estimate) by conducting the averaging in the Earth frame of reference. Doing so would produce a simpler "Earth-frame" geometric factor

$$\bar{R_1^E} = \frac{\bar{R^{\alpha}_{wt}} kre^{kr}}{(1+kr)e^{kr} - 1}. \tag{59}$$

Analytical expression for this factor is given in the Appendix B, and its dependence on kr is illustrated in Fig. 7a. Unlike $\bar{R}_1$, the Earth-frame factor $\bar{R}_1^E$ approaches zero for large negative ranges ($kr \ll -1$). In this regime, the optimal recombination is obtained with weights $c_1 = c_2 = 0.5$, $c_3 = 0$ – i.e., the V-beam vertical velocity estimate is ignored, while the two slant-beam reconstructions are averaged. This solution is intuitive: the estimate affected by the dominant frame-rotation bias should be excluded from the recombination.

Net-zero bias is not the only optimality criterion worth considering. One may instead prefer to minimize RMS bias, $J = \langle|\widetilde{w} - w|^2\rangle = |w_w|^2\langle|\sum R_i|^2\rangle$. Such minimization process would produce a different set of optimal recombination weights, which, however, behave similarly to those derived above (not shown). Yet another approach would be to minimize the average (or worst-case) bias over a particular range of misalignment angles instead of the full $[0, 2\pi]$ interval. For now, we will leave these options as opportunities for future research.

6. Wave-induced biases for the Lagrangian Float

With the general expressions for the wave-induced biases derived in section 4, we can quantify these biases in ADCP velocity measurements obtained from a Lagrangian float with a particular response model derived in DS26 (see section 3b). Unlike the generic analysis of the prior sections, all the results shown below apply only to a specific platform (Lagrangian float) and its response model. Our goal is twofold: estimate the biases inherent in our past and future Lagrangian float observations as well as provide a road map for similar analysis for other platforms.

Generally speaking, the wave-induced biases depend on three primary variables: the wave field, the float depth, and the measurement depth (or range). For a realistic representation of the wave field, we choose the simple Pierson–Moskowitz (PM) surface-elevation spectrum for wind-equilibrium seas (Pierson Jr. and Moskowitz 1964). We assume the waves to be unidirectional and aligned with the ADCP beam pair, which would correspond to a conservative 'worst-case' scenario for bias development. With this assumption, the wave field is uniquely parameterized by the 10-m wind speed, u_{10}. ADCP parameters mimic a five-beam Nortek Signature1000 ADCP with a 25° beam angle, although we consider measurement ranges that may not be achievable by this instrument.

Before presenting the full spectrum-integrated biases, it is useful to examine how individual wave frequencies contribute to the bias. Because both the float response and wave amplitude vary strongly across the frequency range, we define a spectrum-weighted bias density by substituting $a^2 = 2S(f)$ into the bias expressions (36–37), where $S(f)$ is the surface elevation frequency spectrum. This introduces a frequency-dependent bias density scaling parameter

$$\widetilde{U_{SP}}(f) = 2S(f)\omega k e^{2kz_0}. \tag{60}$$

This parameter replaces the monochromatic counterpart (38), and corresponds to a spectral component of the float's own Stokes drift at frequency f and unit bandwidth. In accordance with (36–37), this amplitude modulates the relative bias profiles determined by the ADCP beam geometry to produce the bias density $\widetilde{U_w}(f)$ that determines the bias contribution from a particular frequency component. The net broadband bias is obtained by integration

$$U_w = \int_0^\infty \widetilde{U_w}(f)df. \tag{61}$$

The structure of the bias density $\widetilde{U_w}$ is shaped by both the instrument response and the wave spectrum. Insight into its general behavior can be gained by exploiting the observation that wind-wave spectra usually have a universal high-frequency tail, with only the low-frequency cutoff varying with the wind. For example, Fig. 9a shows the PM spectra for different wind speeds all following the same high-frequency asymptotic $S_{hf}(f) = 5 \times 10^{-4} f^{-5}$ $[m^2/Hz]$ (dashed line). If we compute the bias density $\widetilde{U_w}$ using this universal high-frequency tail, then the full wind-dependent bias is obtained simply by integrating down to the wind-dependent low-frequency cutoff. Therefore, the bias density plots (Fig. 9c-d) alongside the wind-dependent wave spectra (Fig. 9a) clearly indicate which frequencies dominate the bias for a given wind speed and measurement depth. Including the tilt response functions (Fig. 9b) further clarifies where, in the physical space, the float's resonant behavior affects the biases.

These plots show that the largest bias contributions arise from waves with vertical length scales comparable to the depth of the float, i.e. from the band where $kz_0 \sim 1$. For a float at 20 m depth, this corresponds to $f \lesssim 0.1\,\mathrm{Hz}$, the waves excited for wind speeds $u_{10} \gtrsim 10\,\mathrm{m\,s^{-1}}$. The float resonant frequency $f_0 = 0.32\,\mathrm{Hz}$ lies well above this band, so the resonant peak plays only a minor

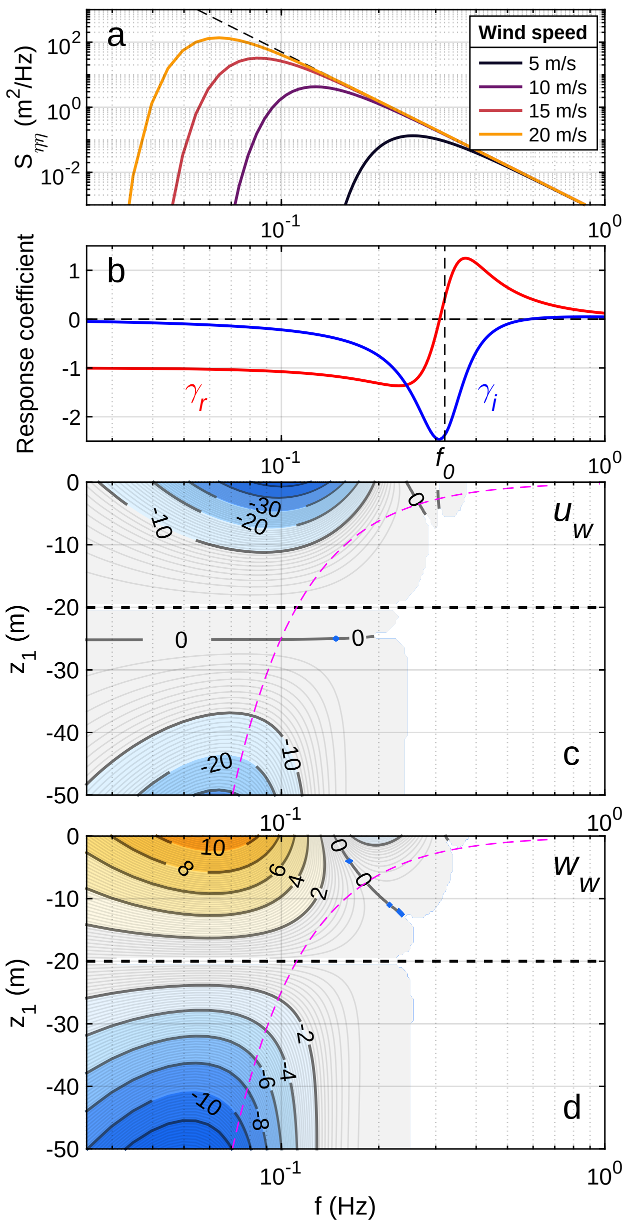

FIG. 9. Frequency dependence of wave-induced biases for Lagrangian float at 20m. (a) Pierson–Moskowitz surface-elevation spectrum at different wind speeds; high-frequency $S_{hf} \sim f^{-5}$ asymptotics is shown in black dashed line; the wave-induced biases are shown for this asymptotic spectrum. (b) Real (red) and imaginary (blue) components of float tilt response coefficient γ based on DS26. Wave-induced bias density for (c) horizontal and (d) vertical velocities obtained from slant-beam ADCP reconstruction for the $S_h f$ spectrum. Bias density contours are labeled in units of $\mathrm{cm\,s^{-1}\,Hz^{-1}}$, note the different contour intervals. Bias density values less than $10^{-5}\,\mathrm{m\,s^{-1}\,Hz^{-1}}$ are not plotted. Magenta dashed lines in (c-d) shows the wave length scale, k^{-1}, for reference. f_0 is the float resonant frequency.

role in ADCP observations of horizontal velocity from 20 m; the resonant response plays a larger role for the vertical velocity bias density (Fig. 9d). Higher frequencies, including the resonant band, have a proportionally stronger impact on the float observations from shallower depths (not shown); however, their net contribution remains limited due to the f^{-5} decay of the wave amplitude spectrum. Lower-frequency waves have a progressively weaker effect on biases despite their high amplitudes, because their vertical scales k^{-1} are large compared to the range of observations r, leading to $kr \approx 0$.

Finally, to characterize the operationally relevant total bias magnitudes, we integrate $\widetilde{U_w}$ over the actual PM spectrum. To summarize the parameter space dependence, we show the biases for a given float depth and varying wind speed, and a given wind speed and varying float depth. We also include the alternative velocity reconstructions discussed earlier – the Earth-frame processing (4c), V-beam measurements (4f), and optimal recombination (5).

Fig. 10 and Fig. 11 show estimates of horizontal velocity biases. As expected, the biases increase with increasing wind speed and typically reach the maximum of up to 4-5 cm/s near the surface for 20 m/s winds. Earth-frame averaging improves the upward-looking biases slightly, while making the downward-looking biases much worse. This behavior could be anticipated from the asymptotic relationship (39) that shows the frame-rotation bias partially offsetting the motion bias for $\gamma_r < 0$.

Vertical velocity biases are shown in Fig. 12 and Fig. 13. They are typically an order of magnitude smaller than horizontal biases, on the order of a few millimeters per second. As discussed in section 4f, the two-beam vertical velocity bias is substantially smaller than the V-beam bias but has a more complex pattern with subsurface maxima of both signs. Optimal beam recombination (section 5) efficiently reduces the vertical velocity bias by another order of magnitude, as could be anticipated from the examples in Fig. 8.

7. Discussion and conclusions

As discussed in SD25, all wave-induced biases considered here arise from the same fundamental mechanism: the superposition of wave orbital motion and the motion of the platform (and hence of the ADCP sampling volume). Because these motions are at least partially coherent, their nonlinear coupling produces aperiodic biases in the measured velocities. For monochromatic wave forcing (or an individual spectral component), the resulting biases generally scale with the geometric mean

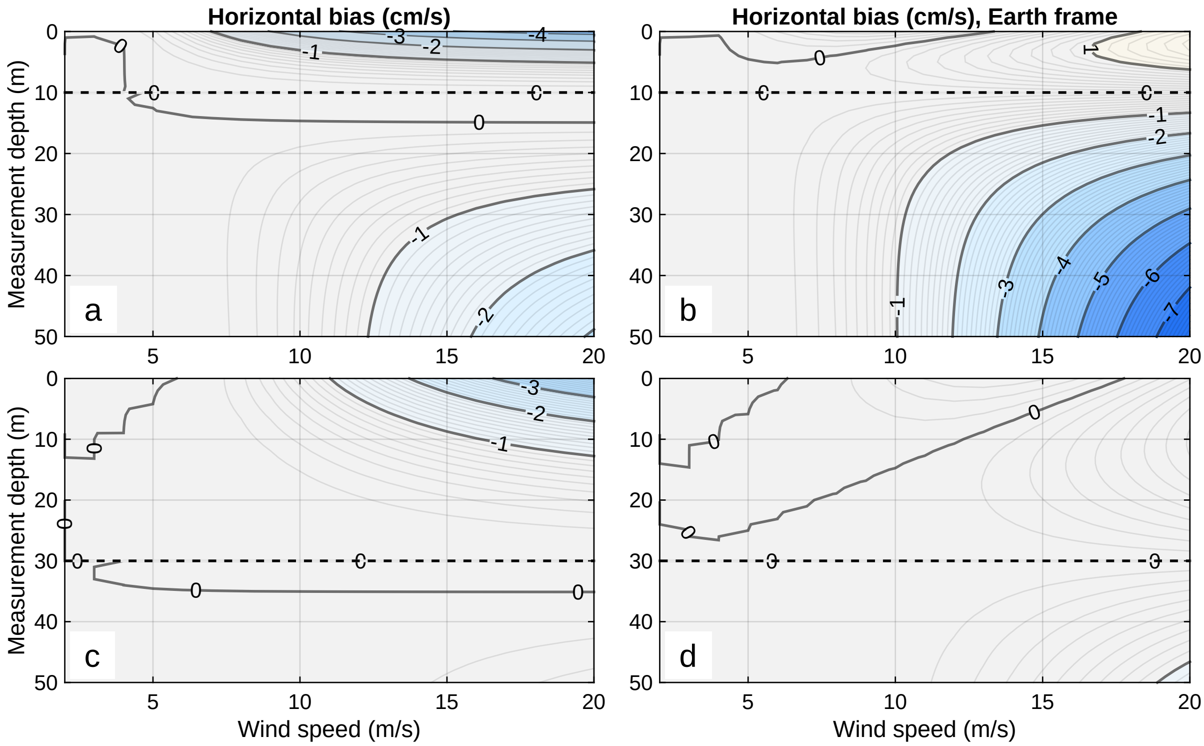

FIG. 10. Wave-induced biases in horizontal velocity measurements from a Lagrangian float situated at 10 m (top row) and 30 m (bottom row) depth as a function of measurement depth and wind speed. The left column (a,c) is the full bias; the right column is the Earth frame bias (excluding the frame rotation). Velocity bias contour labels are are in cm s^{-1}.

of the Stokes drift velocities evaluated at the nominal depths of the platform and the measurement. The detailed bias structure, however, depends critically on the trajectory of the sampling volume through wave phase space, which in turn is controlled by the platform's wave-induced motion and tilt response as well as by the ADCP beam geometry.

Real autonomous platforms can generally be expected to exhibit partially resonant response, leading to both amplification and phase lag of platform's tilt relative to the wave forcing. These effects alter the sampling-volume trajectory through the wave space and therefore modify the coupling between wave orbital motion and the sampling. The resulting phase-averaged biases affect both horizontal and vertical velocity estimates, as described by (36-37). In general, tilt-induced biases in horizontal velocity scale with the real part of the platform tilt transfer function, while biases in vertical velocity scale with its imaginary part. The latter mechanism, absent in

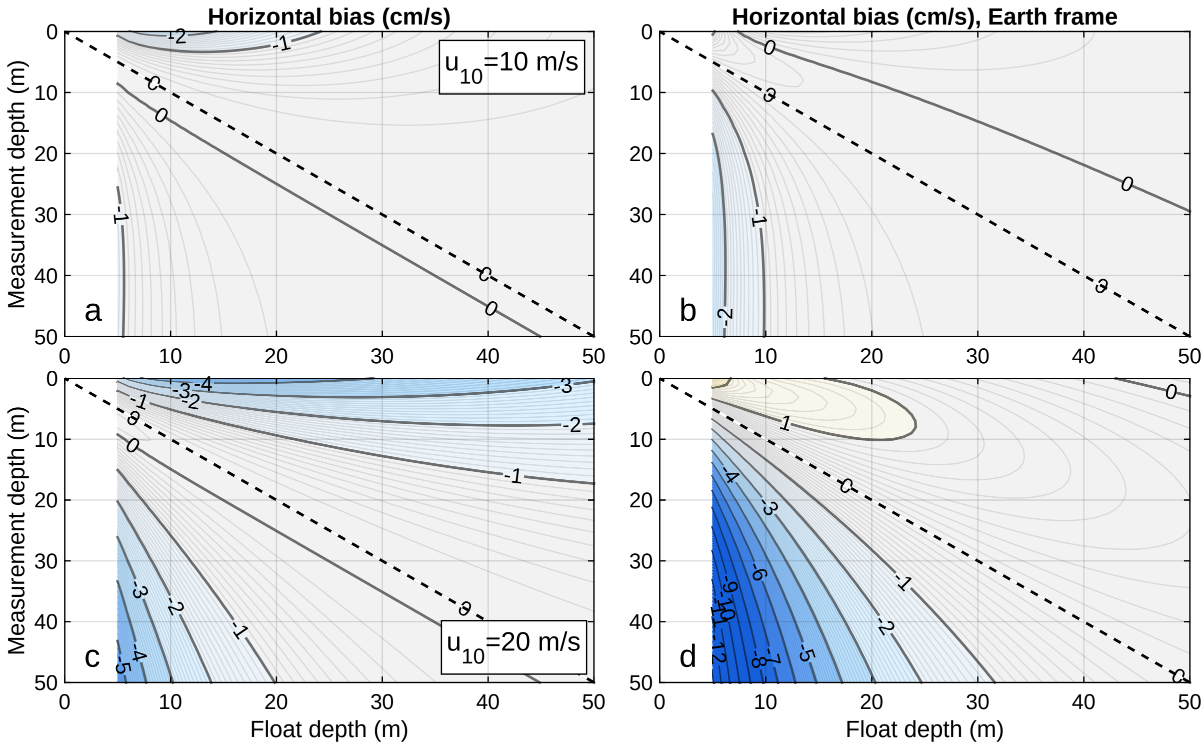

FIG. 11. Same as Fig. 10, but as a function of measurement depth and float depth for moderate (top row) and strong (bottom row) winds.

the in-phase response considered previously, provides a direct pathway for wave-induced vertical velocity bias.

The magnitude and sign of the biases further depend on the relative alignment of the ADCP beams with the direction of wave propagation. Biases are typically largest when a slanted beam pair is aligned with the wave direction (alignment angle $\alpha = 0$), although bias cancellation can occur for particularly favorable ADCP beam spread for a given wavelength (see Fig. 6 and Section e). When the beam pair is orthogonal to the wave direction ($\alpha = 90°$), the horizontal bias vanishes, while the vertical bias remains finite. This directional dependence underscores the importance of beam geometry in interpreting wave-contaminated ADCP observations.

Five-beam ADCPs, which include a vertical beam in addition to the standard slanted beams, offer additional flexibility for mitigating wave-induced vertical velocity bias by providing three independent estimates: two from the slanted beam pairs and one from the vertical beam. Although the vertical-beam estimate alone is typically more strongly biased than the slant-beam reconstruction,

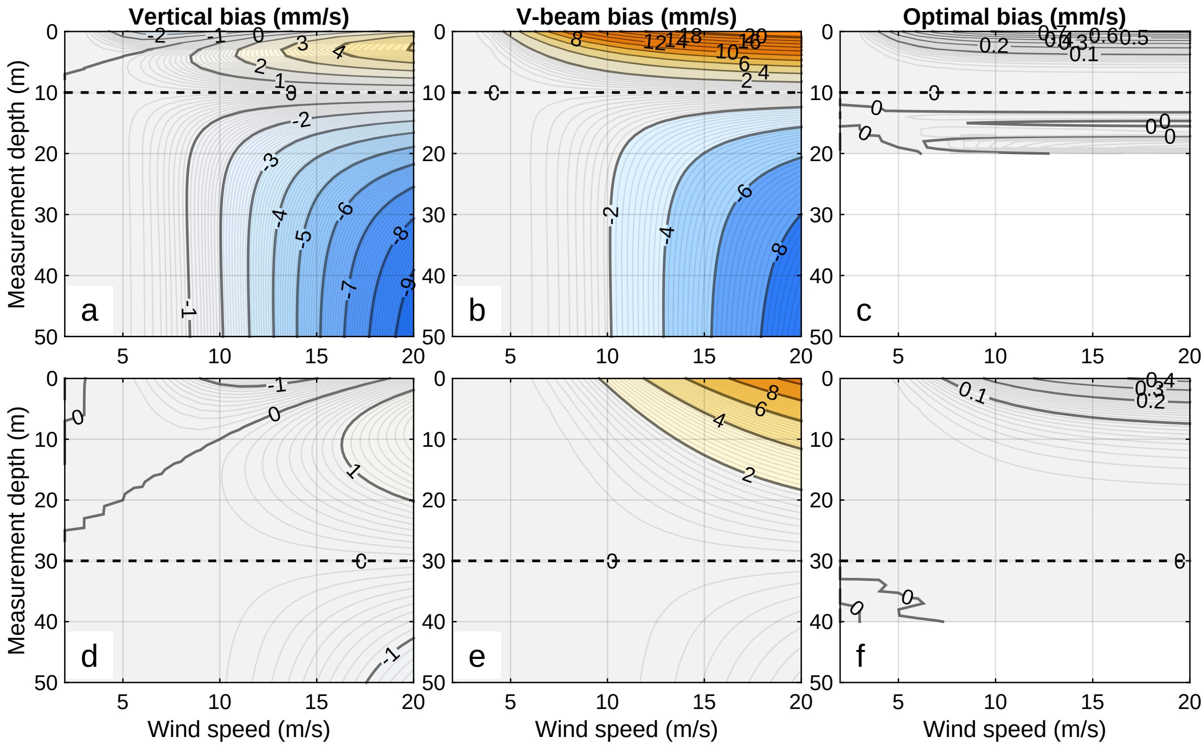

FIG. 12. Wave-induced biases in vertical velocity measurements from a Lagrangian float situated at 10 m (top row) and 30 m (bottom row) depth as a function of measurement depth and wind speed. The left column is the bias of the slant-beam estimate; the middle column is the V-beam bias; the right column bias of the optimal beam recombination (see section 5 for details). Velocity bias contour labels are are in mm s^{-1}.

it is theoretically possible to form an optimal five-beam vertical velocity estimate that is unbiased on average for arbitrary ADCP–wave alignment. This reconstruction must be performed in Fourier space and can be poorly conditioned in certain parameter regimes, leading to noise amplification and potential instability. Whether such unbiased reconstructions are beneficial in practice therefore remains an open question.

In this study, we focus on resonant tilt response and do not explicitly consider resonant or phase-lagged platform motion response. Both here and in SD25, the platform is assumed to be fully Lagrangian, following wave orbital motion without phase lag, attenuation, or resonance (with the notable exception of self-propelled platforms considered in SD25). Under this assumption, the unity motion response function is implicitly assumed in (20). For Lagrangian floats, this approximation has been shown to be valid at spatial scales larger than the float itself ($\gtrsim 1\,m$;

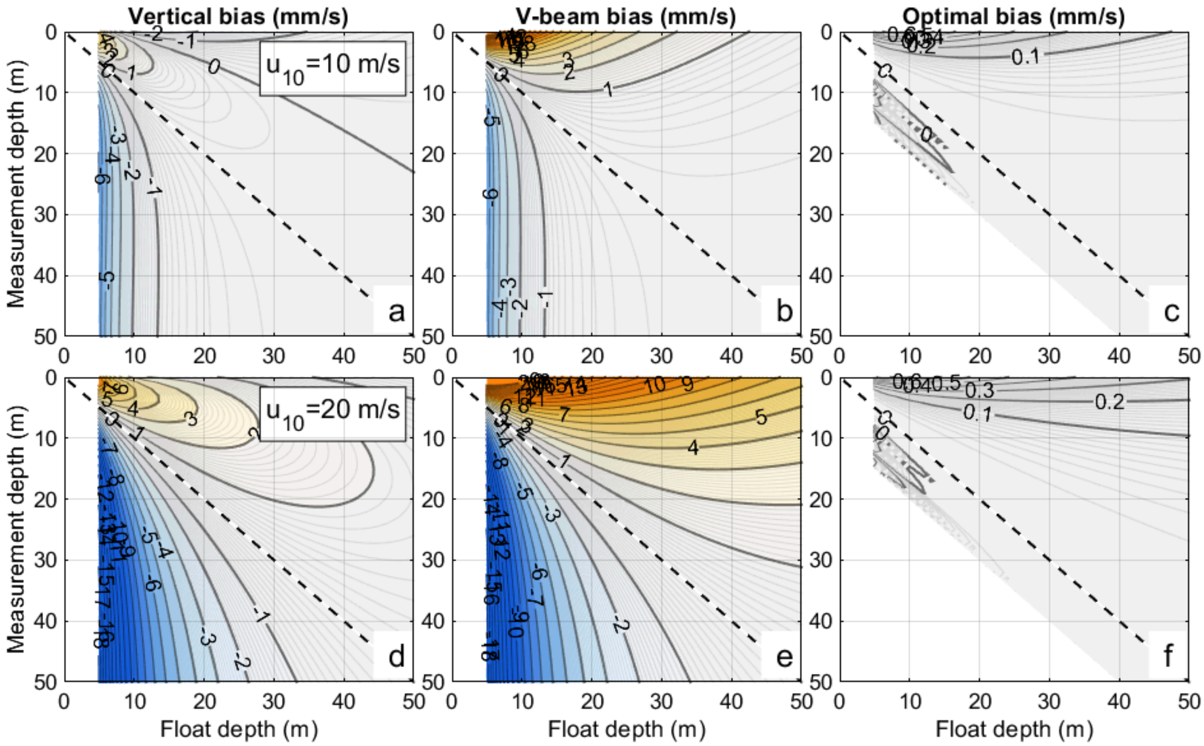

FIG. 13. Same as Fig. 12, but as a function of measurement depth and float depth for moderate (top row) and strong (bottom row) winds.

D'Asaro 2003, 2015). However, this assumption may not hold for all platforms or deployment scenarios. If the platform motion response is itself phase-lagged or frequency dependent, it should be explicitly incorporated into (20), in which case an additional contribution to the vertical velocity bias would arise.

Although the analytical expressions derived here fully characterize wave-induced biases, we remain skeptical that such biases can be reliably removed from observational data in most practical situations, because the wave field parameters, platform orientation, and the platform response functions may be insufficiently constrained. Instead, we suggest that wave-induced biases be treated as an inherent source of uncertainty in autonomous and moored ADCP measurements. These biases can be quantified using the expressions developed here[3], and experimental design measures should be considered to minimize their impact. While wave orbital motions are obviously beyond control, platform configuration, positioning, and dynamic response can sometimes be

[3] A MATLAB implementation of the analytical expressions is provided with the semi-analytical model at `https://github.com/shcher2018/wave-bias`.

modified. As suggested in SD25 and confirmed here, ”an upward-looking ADCP mounted on a subsurface quasi-Lagrangian platform [...] can be expected to have weaker wave-induced biases when observing velocities at a given depth than other configurations”. In addition, shifting the platform tilt resonance toward higher frequencies (i.e., increasing hydrostatic stability) and increasing the quality factor Q to sharpen the response may further reduce wave-induced biases, particularly in vertical velocity estimates. It remains to be seen whether such modifications are feasible from the engineering and operational perspective.

Acknowledgments. This work was supported by NSF Anisotropy and NoSe projects (NSF Awards 2344156, 2421820), the Office of Naval Research ”RIOT” Departmental Research Initiative (N00014-24-1-2720), and by NASA S-MODE project, an EVS-3 Investigation awarded under NASA Research Announcement NNH17ZDA001N-EVS3. We acknowledge helpful discussions with OpenAI’s ChatGPT, which assisted in refining our thinking and presentation. All ideas, conclusions, and remaining errors are our own, though.

Data availability statement. No datasets were generated or analyzed during the current study. MATLAB implementation of the semi-analytical model is freely available at https://github.com/shcher2018/wave-bias under MIT license.

APPENDIX A

Derivation of misaligned ADCP response functions

Consider an ADCP beam-pair oriented at an angle α to the wave propagation direction. The motion bias response function derivation is modified as follows:

$$\overline{U_m^{\pm}} = a^2\omega k e^{k(z_1+z_0)} \langle e^{i(\phi_1^{\pm} - \phi_0)}\rangle = a^2\omega k e^{k(z_1+z_0)}\; e^{\pm i\; k\; r\tan\beta_x} = a^2\omega k e^{k(z_1+z_0)}\; (\cos(kr\tan\beta_x) \pm i\sin(kr\tan\beta_x)) \quad \text{(A1)}$$

$$B^{\pm} = \pm u\cos\alpha\sin\beta + w\cos\beta = \pm\, a^2\omega k e^{k(z_1+z_0)}(\cos(kr\tan\beta_x)\cos\alpha\sin\beta + \sin(kr\tan\beta_x)\cos\beta) \quad \text{(A2)}$$

$$u_{ADCP} = \frac{B^+ - B^-}{2\sin\beta} = a^2\omega k e^{k(z_1+z_0)}\frac{\cos(kr\tan\beta_x)\cos\alpha\sin\beta + \sin(kr\tan\beta_x)\cos\beta}{\sin\beta} \quad \text{(A3)}$$

Thus

$$R_u = \frac{\cos(kr\tan\beta_x)\cos\alpha\sin\beta + \sin(kr\tan\beta_x)\cos\beta}{\sin\beta}. \quad \text{(A4)}$$

For $\alpha = 0$, this simplifies to the original expression. For $\alpha = \pi/2$, $R_u = 0$.

Let's consider the sweeping bias:

$$\bar{U_t^{\pm}} = U_{S0}e^{k(z_0+z_1)}kr(\cos\beta_x)^{-1}e^{\pm i(\beta_x+kr\tan\beta_x)}\langle e^{i\phi_0}(\gamma_r\cos\phi_0-\gamma_i\sin\phi_0)\rangle =$$
$$\frac{1}{2}(\gamma_r-i\gamma_i)U_{S0}e^{k(z0+z1)}kr(\cos\beta_x)^{-1}e^{\pm i(\beta_x+kr\tan\beta_x)}, \quad \text{(A5)}$$

$$B_t^{\pm} = \pm u\cos\alpha\sin\beta + w\cos\beta =$$
$$\frac{1}{2}U_{S0}e^{k(z_0+z_1)}kr(\cos\beta_x)^{-1}[\pm\cos\alpha\sin\beta(\gamma_r\cos(\beta_x+kr\tan\beta_x)\pm\gamma_i\sin(\beta_x+kr\tan\beta_x))+$$
$$\cos\beta(\pm\gamma_r\sin(\beta_x+kr\tan\beta_x)-\gamma_i\cos(\beta_x+kr\tan\beta_x))] =$$
$$\frac{1}{2}U_{S0}e^{k(z_0+z_1)}kr(\cos\beta_x)^{-1}[\pm\gamma_r(\cos\alpha\sin\beta\cos(\beta_x+kr\tan\beta_x)+\cos\beta\sin(\beta_x+kr\tan\beta_x))-$$
$$\gamma_i(\cos\beta\cos(\beta_x+kr\tan\beta_x)-\cos\alpha\sin\beta\sin(\beta_x+kr\tan\beta_x))]. \quad \text{(A6)}$$

From this, we get

$$R_{ut} = \frac{\cos\alpha\sin\beta\cos(\beta_x+kr\tan\beta_x)+\cos\beta\sin(\beta_x+kr\tan\beta_x)}{\sin\beta\cos\beta_x}, \quad \text{(A7)}$$
$$R_{wt} = \frac{\cos\beta\cos(\beta_x+kr\tan\beta_x)-\cos\alpha\sin\beta\sin(\beta_x+kr\tan\beta_x)}{\cos\beta\cos\beta_x}. \quad \text{(A8)}$$

APPENDIX B

Analytic expression for mean response functions

We wish to average the ADCP beam geometric factor over all possible values of alignment angle α,

$$\bar{R_1} = \frac{1}{2\pi}\int_0^{2\pi} R_1(\alpha)d\alpha, \quad \text{(B1)}$$

where

$$R_1 = \frac{(R_w^{\alpha}+R_{wt}^{\alpha}kr)e^{kr}-1}{(1+kr)e^{kr}-1}. \quad \text{(B2)}$$

First, let's obtain the angle averages of the two ADCP response functions:

$$\bar{R}_w^{\alpha} = \frac{1}{2\pi}\int_0^{2\pi} R_w^{\alpha} d\alpha = \frac{1}{2\pi}\int_0^{2\pi} [\cos\phi'_x - \cos\alpha \tan\beta \sin\phi'_x] d\alpha, \tag{B3}$$

where $\phi'_x = \phi' \cos\alpha = kr \tan\beta \cos\alpha$. The integrals can be expressed in terms of the Bessel functions of the first kind,

$$\frac{1}{2\pi}\int_0^{2\pi} \cos\phi'_x d\alpha = \frac{1}{2\pi}\int_0^{2\pi} \cos(\phi' \cos\alpha) d\alpha = J_0(\phi'), \tag{B4}$$

$$\frac{1}{2\pi}\int_0^{2\pi} \cos\alpha \sin\phi'_x d\alpha = \frac{1}{2\pi}\int_0^{2\pi} \cos\alpha \sin(\phi' \cos\alpha) d\alpha = J_1(\phi'), \tag{B5}$$

therefore

$$\bar{R}_w^{\alpha} = J_0(\phi') - J_1(\phi') \tan\beta. \tag{B6}$$

Next,

$$\bar{R}_{wt}^{\alpha} = \frac{1}{2\pi}\int_0^{2\pi} R_{wt}^{\alpha} d\alpha = \frac{1}{2\pi}\int_0^{2\pi} [\frac{\cos(\beta_x + \phi'_x)}{\cos\beta_x} - \cos\alpha \tan\beta \frac{\sin(\beta_x + \phi'_x)}{\cos\beta_x}] d\alpha. \tag{B7}$$

Transforming the integrand to eliminate β_x:

$$\frac{\cos(\beta_x + \phi'_x)}{\cos\beta_x} = \frac{\cos\beta_x \cos\phi'_x - \sin\beta_x \sin\phi'_x}{\cos\beta_x} = \cos\phi'_x - \cos\alpha \tan\beta \sin\phi'_x, \tag{B8}$$

$$\cos\alpha \tan\beta \frac{\sin(\beta_x + \phi'_x)}{\cos\beta_x} = \cos\alpha \tan\beta \frac{\sin\beta_x \cos\phi'_x + \cos\beta_x \sin\phi'_x}{\cos\beta_x} = \cos\alpha \tan\beta \sin\phi'_x + \cos^2\alpha \tan^2\beta \cos\phi'_x, \tag{B9}$$

and using

$$\frac{1}{2\pi}\int_0^{2\pi} \cos^2\alpha \cos\phi'_x d\alpha = \frac{1}{2\pi}\int_0^{2\pi} \cos^2\alpha \cos(\phi' \cos\alpha) d\alpha = \tfrac{1}{2}(J_0(\phi') - J_2(\phi')) \tag{B10}$$

We obtain

$$\bar{R}_{wt}^{\alpha} = J_0(\phi') - 2J_1(\phi') \tan\beta - \tfrac{1}{2}(J_0(\phi') - J_2(\phi')) \tan^2\beta. \tag{B11}$$

Using the recurrence relation $J_2(x) = 2x^{-1}J_1(x) - J_0(x)$, this can be simplified as

$$\bar{R}_{wt}^{\alpha} = J_0(\phi')(1-\tan^2\beta) + J_1(\phi')(\frac{1}{kr} - 2)\tan\beta. \tag{B12}$$

Finally,

$$\bar{R_1} = \frac{[J_0(\phi') - J_1(\phi')\tan\beta + (J_0(\phi')(1-\tan^2\beta) + J_1(\phi')(\frac{1}{kr}-2)\tan\beta)kr]e^{kr} - 1}{(1+kr)e^{kr} - 1} = \frac{[J_0(\phi')(1+kr(1-\tan^2\beta)) - 2J_1(\phi')\tan\beta]e^{kr} - 1}{(1+kr)e^{kr} - 1}. \tag{B13}$$

Similarly, the Earth-frame geometric factor can be calculated as

$$\bar{R}_1^E = \frac{[J_0(\phi')kr(1-\tan^2\beta) + J_1(\phi')(1-2kr)\tan\beta]e^{kr}}{(1+kr)e^{kr} - 1}. \tag{B14}$$

References

Bretherton, F. P., 1962: The motion of rigid particles in a shear flow at low Reynolds number. *Journal of Fluid Mechanics*, **14**, 284–304, https://doi.org/10.1017/S002211206200124X.

Comby, C., S. Barrillon, J.-L. Fuda, A. M. Doglioli, R. Tzortzis, G. Grégori, M. Thyssen, and A. A. Petrenko, 2022: Measuring vertical velocities with adcps in low-energy ocean. *Journal of Atmospheric and Oceanic Technology*, **39**, 1669–1684, https://doi.org/10.1175/JTECH-D-21-0180.1.

D'Asaro, E., 2015: Surface wave measurements from subsurface floats. *Journal of Atmospheric and Oceanic Technology*, **32 (4)**, 816–827, https://doi.org/10.1175/JTECH-D-14-00180.1.

D'Asaro, E. A., 2003: Performance of autonomous lagrangian floats. *Journal of Atmospheric and Oceanic Technology*, **20**, 896–911, https://doi.org/10.1175/1520-0426(2003)020%3C0896:POALF%3E2.0.CO;2.

D'Asaro, E. A., and A. Y. Shcherbina, 2026: The motion and tilts of subsurface floats due to surface waves. *Journal of Atmospheric and Oceanic Technology*.

Jeffery, G. B., 1922: The motion of ellipsoidal particles immersed in a viscous fluid. *Proceedings of the Royal Society of London. Series A*, **102**, 161–179, https://doi.org/10.1098/rspa.1922.0078.

Longuet-Higgins, M. S., 1986: Eulerian and Lagrangian aspects of surface waves. *Journal of Fluid Mechanics*, **173**, 683–707, https://doi.org/10.1017/S0022112086001325.

Pierson Jr., W. J., and L. Moskowitz, 1964: A proposed spectral form for fully developed wind seas based on the similarity theory of S. A. Kitaigorodskii. *Journal of Geophysical Research (1896-1977)*, **69 (24)**, 5181–5190, https://doi.org/https://doi.org/10.1029/JZ069i024p05181.

Shcherbina, A. Y., and E. A. D'Asaro, 2025: Wave-induced biases in adcp measurements from quasi-lagrangian platforms. *Journal of Atmospheric and Oceanic Technology*, **42**, 545–565, https://doi.org/10.1175/JTECH-D-24-0046.1.

Shcherbina, A. Y., E. A. D'Asaro, and S. Nylund, 2018: Observing finescale oceanic velocity structure with an autonomous Nortek acoustic doppler current profiler. *Journal of Atmospheric and Oceanic Technology*, **35**, 411–427, https://doi.org/10.1175/JTECH-D-17-0108.1.